CORA Cork Open Research Archive
Cartlann Taighde Oscailte Chorcaí

Title	Operando color-coding of reversible lithiation and cycle life in batteries using photonic crystal materials
Authors	Lonergan, Alex;Gulzar, Umair;Zhang, Yan;O'Dwyer, Colm
Publication date	2023-12-27
Original Citation	Lonergan, A., Gulzar, U., Zhang, Y. and O'Dwyer, C. (2023) 'Operando color-coding of reversible lithiation and cycle life in batteries using photonic crystal materials', ECS Sensors Plus, 2(4), 045401 (11pp). https://doi.org/10.1149/2754-2726/ad15a0
Type of publication	Article (peer-reviewed)
Link to publisher's version	10.1149/2754-2726/ad15a0
Rights	© 2023, the Authors. Published on behalf of The Electrochemical Society by IOP Publishing Limited. This is an open access article distributed under the terms of the Creative Commons Attribution 4.0 License (https://creativecommons.org/licenses/by/4.0/), which permits unrestricted reuse of the work in any medium, provided the original work is properly cited. - https://creativecommons.org/licenses/by/4.0/
Download date	2026-11-17 08:50:01
Item downloaded from	https://hdl.handle.net/10468/15832



University College Cork, Ireland
Coláiste na hOllscoile Corcaigh

ECS Sensors Plus

The Electrochemical Society
Advancing solid state & electrochemical science & technology

OPEN ACCESS

Operando Color-Coding of Reversible Lithiation and Cycle Life in Batteries Using Photonic Crystal Materials

To cite this article: Alex Lonergan *et al* 2023 *ECS Sens. Plus* **2** 045401

View the article online for updates and enhancements.

You may also like

- Towards Perfect Vertical Photonic Band Gap Confinement in a Photonic Crystal Slab
Nobuhiko Susa
- Methods to Tune the Optical Response of Porous Photonic Crystal Structures
Alex Lonergan and Colm O'Dwyer
- Operando Photonic Stopband Monitoring of Lithium-Ion Battery Electrodes
Alex Lonergan, Umair Gulzar, Yan Zhang et al.

This content was downloaded from IP address 109.78.119.40 on 29/04/2024 at 10:03

ECS Sensors Plus, 2023 **2** 045401

Operando Color-Coding of Reversible Lithiation and Cycle Life in Batteries Using Photonic Crystal Materials

Alex Lonergan,[1] Umair Gulzar,[1] Yan Zhang,[1] and Colm O'Dwyer[1,2,3,4,z]

[1]*School of Chemistry, University College Cork, Cork, T12 YN60, Ireland*
[2]*Micro-Nano Systems Centre, Tyndall National Institute, Lee Maltings, Cork, T12 R5CP, Ireland*
[3]*AMBER@CRANN, Trinity College Dublin, Dublin 2, Ireland*
[4]*Environmental Research Institute, University College Cork, Lee Road, Cork T23 XE10, Ireland*

Innovative new materials are consistently emerging as electrode candidates from lithium-ion and emerging alternative battery research, promising high energy densities and high-rate capabilities. Understanding potential structural changes, morphology evolution, degradation mechanisms and side reactions during lithiation is important for designing, optimizing and assessing aspiring electrode materials. In-situ and operando analysis techniques provide a means to investigate these material properties under realistic operating conditions. Here, we demonstrate operando spectroscopic sensing using photonic crystal-structured electrodes that uses the optical transmission spectrum to monitor changes to the state of charge or discharge during lithiation, and the change to electrode structure, in real-time. Photonic crystals possess a signature optical response, with a photonic bandgap (or stopband) presenting as a structural color reflection from the material. We leverage the presence of this photonic stopband, alongside its intricate relationship to the electrode structure and material phase, to correlate electrode lithiation with changes to the optical spectrum during operation. We explore the optical and electrochemical behavior of a TiO_2 anode in a lithium-ion battery, structured as a photonic crystal. The operando optical sensing demonstrated here is versatile and applicable to a wide range of electrochemical electrode material candidates when structured with ordered porosity akin to a photonic crystal structure.
© 2023 The Author(s). Published on behalf of The Electrochemical Society by IOP Publishing Limited. This is an open access article distributed under the terms of the Creative Commons Attribution 4.0 License (CC BY, http://creativecommons.org/licenses/by/4.0/), which permits unrestricted reuse of the work in any medium, provided the original work is properly cited. [DOI: 10.1149/2754-2726/ad15a0]

Manuscript submitted July 31, 2023; revised manuscript received November 9, 2023. Published December 27, 2023.

Supplementary material for this article is available online

The growing popularity of smartphones, electric vehicles and wearable electronic devices, alongside their associated high energy demands, has driven the research for lithium-ion battery (LIB) materials towards achieving higher energy densities, higher cycling stability, longer lifespans, safer battery cells, lighter and more flexible designs.[1–3] Future energy storage devices require highly energy dense materials which can be manufactured into versatile designs to support emerging technological innovation.[4,5] Research attempts to facilitate these requirements commonly explore alternative electrode materials for both the anode[6,7] and the cathode.[8,9] Another approach focuses on exploring novel geometries or material dimensions, with particular emphasis on nano-sized architectures, for the electrode materials.[10,11] Incorporating nano-sized features into the electrode design has reported advantages of shorter ion diffusion lengths with a larger surface area exposed, improved rate capability from the increased electrolyte/electrode interface and better accommodation of material volume changes due to inherent porosity or particle spacing.[12,13]

Mainstream commercial uptake of these alternative electrode materials or designs requires detailed information on side reactions, degradation mechanisms, particle cracking, morphology evolution, material phase changes and state of charge heterogeneity in order to assess the health and long term stability of these potential electrodes in functioning cells.[14–16] In-situ and operando characterisation techniques offer pathways to assess the battery performance and electrode material evolution non-invasively, allowing for this information to be obtained under realistic operating conditions by maintaining the sealed battery environment during analysis.[17–19] This is contrary to ex situ or post-mortem analytical techniques which deconstruct the battery cell for analysis, introducing the possibility of material contamination which may not provide an accurate description of performance.[20]

Development and progress related to in situ and operando techniques in the literature has taken many forms, cleverly utilising a variety of different analytical techniques to probe aspects of LIB behavior. In-situ X-ray diffraction (XRD) has been used to track structural changes and reversibility in anatase TiO_2 electrodes[21] and assess the crystallinity and identify metastable phases in silicon nanowires.[22] In-situ and operando Raman spectroscopy can monitor the intensity and position of phonon modes which has been used to identify structural phase transitions (or lack thereof) in TiO_2 nanowire and nanoparticle electrodes[23] or pinpoint the lithiation potential in doped silicon anodes using the transition from crystalline to amorphous silicon as an indicator.[24] Operando atomic force microscopy (AFM) has been used to study dendrite growth on lithium metal electrodes[25] or assess the mechanical properties of silicon anodes during lithiation processes.[26] A myriad of other techniques used in the literature for in-situ and operando studies include nuclear magnetic resonance (NMR),[27] scanning electron microscopy (SEM),[28] transmission electron microscopy (TEM),[29] fourier transform infrared (FTIR) spectroscopy[30] and acoustic ultrasound transmission,[31] to name just a few. Critically, each of these techniques offers an insight into LIB operation which cannot be obtained through conventional ex-situ methods.

Recently, operando and in-situ optical characterisation techniques have begun to emerge. Optical scattering intensity from electrode materials and particles has been used to track phase transitions and state of charge in specific materials.[32,33] An optical operando technique utilizing line scanning confocal reflectance microscopy, where reflected light was used to build images of particle agglomerates in electrode systems from an infrared laser source scanning across the surface, was proposed to study electrode particle volume changes, heterogeneities in lithium occupancy and concentration gradients in electrolyte.[34] Operando optical reflection microscopy has recently been used to image particles alongside investigating light-induced charging for photobattery materials such as $Li_xV_2O_5$ electrodes.[35] Optical fibre Bragg grating sensors have been embedded in coin cells in efforts to provide non-invasive operando assessment of chemo-mechanical stress in electrode materials.[36] Cross-sectional optical microscopy images of lithium-ion full cells have been used to provide in situ insights into lithiation-linked color changes and electrode thickness evolution.[37] In-situ UV–vis spectroscopy has been shown to provide useful supplementary characterisation to electrochemical processes by

[z]E-mail: c.odwyer@ucc.ie

determining charge storage mechanisms and tracking of changes in material oxidation states.[38] Adopting optical probes provides many opportunities to evaluate mechanical/volumetric changes, interfacial species changes, electrolyte composition and absorption characteristics related to electronic processes with materials, to name a few possibilities. While invasive probes prove useful in evaluation of cell-level state of health in batteries, there are challenges in assessing how active material interconnection and changes can be tracked in real-time, a problem that lies between spectroscopic identification of surface species or changes in electrode-level responses.

Here, we take an approach to develop an operando electrode characterisation technique that exploits the unique characteristics of photonic crystals (PhCs), where the periodicity in material refractive index creates a photonic band gap (full inhibition) or photonic stopband (partial inhibition), somewhat analogous to the electronic band gap in semiconducting materials, to disallow propagation of certain frequencies of light. More specifically, we leverage the presence of the photonic stopband in inverse opal (IO) structured TiO_2 anodes to sense and monitor the behavior of the electrode non-destructively during reversible lithitation-induced changes to the interconnected active material. Electrodes incorporating an IO PhC design have been explored to a large degree in the literature, and serve as model electrodes for investigating porosity and the influence of interconnection between active materials without binders or additives.[39–42] Electrodes structured as IOs are thought to benefit from increased access to electrolyte, higher mass transport and less tortuosity in ion diffusion paths compared to bulk materials,[40] thus IO structures are often incorporated into electrode designs where high charge/discharge rate capabilities are desirable.[42–44] Active materials which are especially prone to volumetric expansion, such as Si and Ge, have used the porosity of the IO template for buffering against the strain induced by repeated lithium insertion/removal.[45–49] The inherent porosity of the IO scaffold also makes these structures attractive candidates as composites electrodes, combining different active electrode materials and investigating the interplay in their electrochemical behavior.[50–53] This also applies in the case of TiO_2 IOs, which are renowned for their long-term structural stability as anodes,[42] with literature applications opting for composite electrode configurations using TiO_2 IOs as stable structural supports for higher performance active materials which may be more prone to structural instability with cycling.[54,55]

However, these IO PhCs are much more than just a simple structural template and are renowned for their ability to manipulate specific frequencies of light[56–58] as the periodic dielectric structure establishes a "structural color" reflection from the PhC surface.[59,60] The associated structural color of an individual PhC is sensitive to the periodicity of the repeating structure and the refractive indices of the constituent materials. Importantly, any changes to these parameters result in changes to the wavelength reflected from the surface, allowing these materials to act as sensors.[56–58] There has been a myriad of applications which have been developed utilizing the structural color of a PhC material. Solvent detectors[61,62] oil detectors,[63] glucose sensors,[64] anti-counterfeiting marks,[65] relative humidity-based motion sensors,[66] smart windows with temperature sensitivity,[67] slow photon-enhanced photocatalysis[68,69] and solar cell reflector layers[70] are just some of the applications from a broad literature library of published applications which make specific use of the structural color of various different PhC designs. The structural color inherent to IO PhC materials is a key component to the unique potential of the technique proposed here. Electrodes which adopt a periodic PhC can exploit this observable structural color to provide information on battery material behavior, non-destructively and without specialised equipment, provided the battery cell was constructed to facilitate optical observation of the electrode material. Recently, using the shrinking and swelling of PhC hydrogels, changes in structural color have been used to track water content present in solid-state electrolyte in zinc-air batteries,[71] demonstrating the capability of a PhC-based optical sensing system.

While ordered and interconnected porous materials such as inverse opals have shown promising and stable responses in LIBs using a range of cathode and anode materials, there remains some open questions on how such electrodes vary during cycling since it has been assumed that porosity (acknowledging the gravimetric and volumetric energy density penalty) is believed to facilitate the typical volumetric change, while the interconnected nature maintains electrical conductivity.[57] But mechanical deformation accommodation must also occur if that is the case, or a change to periodicity must accompany large volume changes. Similar queries arise for random porous materials and the nature of material packing, ionic and electronic conductivity and the benefits of non-tortuous porosity. The marriage of photonic crystal and electrochemical and physical processes is examined here as an operando tracking probe to determine how they behave during cycling. The idea for this concept has been proposed for some time,[72] though there has yet to be a practical implementation for the technique. In this work, we showcase a new operando characterization technique for LIBs which directly exploits this phenomenon. Our results suggest that for TiO_2 IO electrodes, the wavelength position and transmission intensity of the photonic stopband is intimately linked to the degree of lithiation of the electrode. The degree of light transmission intensity, as evidenced by operando spectra, is found to track with the operating voltage for both charge and discharge processes; a cyclical variation in the optical transmission emerges during charging and discharging. Additionally, operando transmission spectra recorded during cyclic voltammetry and galvanostatic charge/discharge cycles of TiO_2 IO electrodes exhibit a consistent red-shifting of the photonic stopband energy during cycling. We discuss the significance of these results, correlating the shifts in the photonic stopband to the physical properties of the IO electrode. Most notably, the operando technique explored here is not restricted to just TiO_2 IO electrodes; the method is versatile and applicable to a wide range of electrochemically active electrode materials that can be structured to feature a photonic stopband.

Experimental

Preparation of polystyrene artificial opal templates.— Polystyrene spheres in an aqueous suspension were used to form the sacrificial artificial opal templates for the IO structure. Monodisperse sphere suspensions, with a concentration of 2.5 wt% polystyrene, were purchased from Polysciences Inc. and used, as received, for forming the opal templates via dip-coating. In this work, spheres were purchased with diameters in the ranges of approximately 370–380 nm and 490–500 nm, depending on the application. A sulfate ester used in the preparation process of the polystyrene spheres bestowed a slight negative charge to the spheres. Opal templates were prepared on glass substrates which had been pre-cut into 2×1 cm^2 pieces. The glass substrates were first cleaned via successive ultrasonication (at a frequency of 40 kHz) in acetone (reagent grade 99.5%; Sigma-Aldrich), isopropyl alcohol (reagent grade 99.5%; Sigma-Aldrich) and deionised water, for 5 min each, in order to remove any dust or dirt particles by physical agitation. Following the cleaning process, a 1×1 cm^2 surface on the glass substrate was exposed to UV-Ozone treatment using a Novascan PSD Pro Series cleaner for a period of 1 h, in order to promote surface hydrophilicity, immediately prior to immersion in the aqueous sphere suspension. Treated substrates were dip-coated into pre-heated vials of sphere suspension at a rate of 1 mm min^{-1} which were maintained at a temperature of approximately 50 °C. An MTI PTL-MM01 dip-coater was used for all dip-coating processes. Glass substrates were immersed at a slight incline angle (~10°–20°) to the vertical in order to improve the adhesion of the polystyrene spheres to the surface. Upon immersion into the suspension, the substrate was held still for 5 min to the allow the surface of the suspension to settle and allow a stable meniscus to form with the substrate. Finally, the substrate was withdrawn from the suspension at a rate of 1 mm min^{-1} with the polystyrene spheres arranging themselves into an ordered colloidal crystal template during extraction.

Sol-gel infiltration and preparation of TiO_2 inverse opals.— TiO_2 inverse opals were prepared using the sol-gel synthesis technique to infiltrate the voids in a prepared sacrificial opal template. In this technique, a liquid (sol) precursor is introduced into the air voids of an opal template. Ambient moisture or applied heat to the infiltrated template allows the sol to hydrolyse, condense or crosslink to form a solid material (gel) which resides in the interstitial voids of the opal template. Annealing the samples at high temperatures is often performed to create crystalline materials. For the TiO_2 IOs prepared in this work, a 0.1 M $TiCl_4$ solution in isopropyl alcohol was utilised as the sol-gel precursor. A titanium (IV) chloride tetrahydrofuran complex ($TiCl_4$·2THF 97%; Sigma-Aldrich) was used as the source of $TiCl_4$; the precursor solution was magnetically stirred for 24 h before use, at which point the solution was clear in color. For the sol-gel infiltration process, the $TiCl_4$ solution was drop-cast using a syringe onto opal templates. One or two drops of the precursor was applied, just enough to adequately wet the entire surface of the photonic crystal. Special care was taken to not flood the sample with excess precursor, which can create solid layers of material which may sit atop any potential IO structure. The sacrificial opal template was subsequently removed via calcination in air at 450 °C for 1 h with a heating ramping rate of 5 °C min^{-1}. The high temperature allowed for both the removal of the opal template and for the crystallization of the TiO_2 material to anatase phase TiO_2.

Microscopy and materials characterisation.—Scanning electron microscopy (SEM) was carried out using a Zeiss Supra 40 high resolution SEM at typical accelerating voltages of 15–20 kV. The instrument was used to analyse the morphology of the opals and IO PhCs, and the metal film morphology or thickness. Dimensional analysis for feature size distributions from SEM images were measured using IMAGEJ software. Microscopy analysis was performed on selected samples before and after electrochemical cycling. Energy dispersive X-ray spectroscopy (EDX) analysis was also performed on the same SEM instrument using an accelerating voltage of 15 kV. EDX line scan measurements were obtained in several directions across the surface. EDX analysis was particularly useful for detecting the presence of residual electrolyte salt in post-cycling images, often presenting as enlarged IO walls. EDX analysis could screen for elements present in the electrolyte salt and ensure that post-cycling images were free from any salt contamination, please see Supplementary Materials Figs. S11 and S12 for further details.

Raman scattering spectroscopy for identifying material phase.—Raman scattering analysis was used to characterise the prepared TiO_2 IO films. The analysis was useful for identifying the material phase of TiO_2, with modes corresponding to anatase phase TiO_2 detected here (see Supplementary Materials Fig. S10 for more details). Raman scattering spectroscopy was carried out using a Renishaw InVia Raman Spectrometer with a 30 mW Ar^+ laser with an excitation wavelength of 532 nm. The beam was focused using a 40× objective lens and collected using a RenCam CCD camera.

Deposition of conductive metal layers onto TiO_2 inverse opals.—Nickel metal layers were deposited over the surface of TiO_2 IOs, formed on glass substrates, in order to provide a conductive layer for the electrode. A thickness of 20 nm of Ni was used for the electrodes in this work, providing a good balance between the conductivity and the optical transmission of the electrode. The metal films were deposited via physical vapour deposition using a Quorum 150 T S magnetron sputtering system. The thickness of the film deposited could be measured using a built-in film thickness monitor. The Ni metal target was purchased from Ted Pella Inc. featuring a material purity of 99.99%. The magnetron sputtering system featured a shutter system which could be used to clean the surface of the Ni target prior to deposition, a necessary precaution in the case of Ni metal which is prone to oxidation. All films were sputtered under an inert atmosphere of high purity to prevent the any reaction between the metal particles and the gas atmosphere. In this case, argon gas (>99.995%) was used as the inert gas for sputtering. The possibility of using transparent conductive oxides, such as fluorine-doped tin oxide, as substrates was explored and found to be incompatible with this measurement system due to alloying lithiation-induced opacity, see Supplementary Materials Fig. S1 for more details.

Creating the transparent battery cell for recording operando spectra.—Conventional coin and pouch cells used in traditional and non-specialised lithium-ion battery research could not be used for analysis in this work as they do not possess the capability to record optical spectra, often been constructed and encapsulated in stainless steel. In order to record optical spectra consistently and to ensure compatibility with our optical system, a custom battery cell was designed to facilitate optical measurements. A cylindrical glass vial with a diameter of 2.5 cm and a height of 5 cm was used as the main body of the transparent cell, allowing for light to pass through and be collected by a spectrometer. A custom 3D printed cap was designed using AutoCAD to tightly to fit over the top of the system, while also gripping the electrode and ensuring it remained upright during analysis. Two protruding holes from the top of the cap were used to allow for electrical wire connections to the electrodes. A stereolithography (SLA) vat polymerisation 3D printer was used for constructing 3D models. Here, a Formlabs Form 2 3D printer, featuring a 250 mW laser operating at 405 nm, was used. High temperature resistant resin from Formlabs was used, on merit of its strong structural composition and high deflection temperature >210 °C, in order to resist possible degradation from electrolyte vapor during operation. A hot glue gun and Kapton tape (Bemis Company, Incorporated) were used to seal openings in the cell and keep it hermetically sealed. All cells were assembled in an inert atmosphere, in this case inside a glovebox in an argon environment.

Optical transmission measurements.—Optical transmission spectra were recorded using an Ocean Optics Inc. USB2000 + VIS-NIR-ES UV-visible spectrometer which features an operational wavelength range of 350–1000 nm and records optical data points in intervals of approximately 0.4 nm. An unpolarised tungsten-halogen lamp, with an operational wavelength range of 400–2200 nm purchased from Thorlabs Inc., was used as the broadband light source for recording spectra. For spectra recorded in air, 100% transmittance was normalised to the transmission spectrum of a clean blank piece of glass, allowing the spectra of TiO_2 IOs on glass to be recorded relative to the spectrum of glass. Similarly, for the spectra recorded in 0.1 M $LiPF_6$ electrolyte, 100% transmittance was normalised to the transmission spectrum of a clean blank piece of glass suspended upright in the electrolyte. For all spectra recorded in this work, the angle of incidence between the normal from the photonic crystal surface and the incident light was fixed at 0° incidence. For recording measurements over long periods of time (e.g. operando spectra recorded over many different electrochemical cycles), transparent battery cells were clamped in place to prevent any movement of the sample. This is an important consideration as there is some spectral variance experienced between different sample spots on the same IO electrode; clamping the cell in place ensured that the spectra were consistent and, importantly, recorded from the exact same sample spot.

Electrochemical analysis.—Electrochemical testing was carried out using a Biologic VSP potentiostat/galvanostat instrument. TiO_2 IO electrodes were tested in a half-cell arrangement, as the working electrode, with lithium metal acting as the counter and reference electrode. The mass loadings for the TiO_2 IO electrodes were within the range 0.1–0.2 mg. Figure 1b shows the typical half-cell configuration used in this work, with the half-cell setup tailored for optical transmission. A flooded-cell design, with an excess of electrolyte of approximately 5–6 mL, was used for all of the electrochemical tests

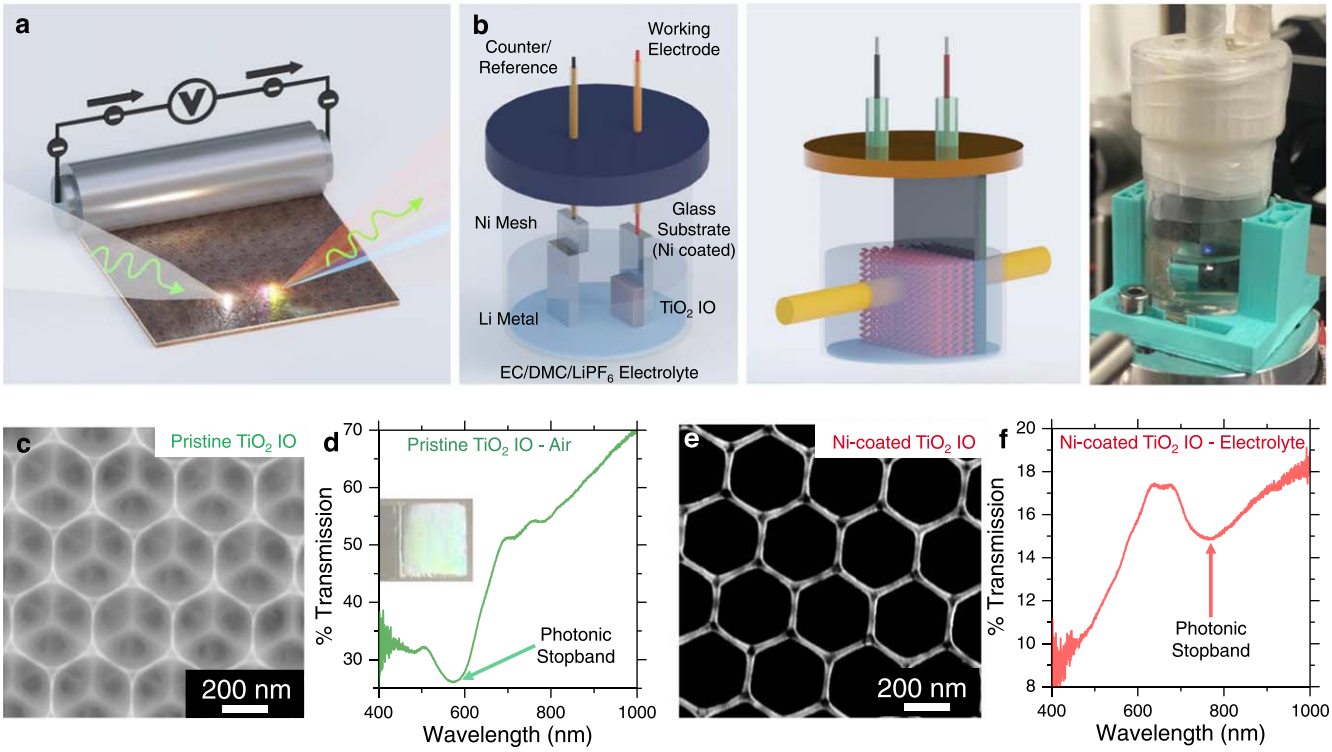


Figure 1. Operando spectroscopy and photonic crystal battery electrodes. (a) The operando technique for photonic crystal LIB electrodes obtains simultaneous optical spectra and electrochemical charge-discharge data from the ordered macroporous TiO_2 inverse opal electrode. (b) The glass battery cell casing uses a half-cell configuration and allows light transmission through the electrode. Lithium metal is used as the counter and reference electrode, with sputtered Ni forming the current collector to the working electrode. (c) Scanning electron microscopy of a typical TiO_2 IO used as an electrode prior to any modifications shows the highly ordered interconnected nature of the IO material. (d) The optical transmission spectrum of a typical unmodified TiO_2 IO prepared using 350 nm polystyrene opal spheres as a sacrificial template, showing a photonic stopband centred at approximately 573 nm. (e) SEM image of a typical TiO_2 IO following magnetron sputter deposition of 20 nm of Ni metal onto the surface to form the current collector. (f) A TiO_2 IO following deposition of 20 nm of Ni metal and immersion of the IO into ethylene carbonate:dimethyl carbonate:$LiPF_6$ battery electrolyte, showing a red-shifted photonic stopband centred at approximately 766 nm.

in this work. The electrolyte was purchased from Sigma-Aldrich as a 1 M solution of $LiPF_6$ salt dissolved in a 1:1 (v/v) mixture of ethylene carbonate and diethyl carbonate. For both galvanostatic and cyclic voltammetry tests, the voltage ranges were set to 1.0–3.0 V. CV scan rates were varied from 0.1–0.3 mV s^{-1}, depending on the application. For galvanostatic tests, C-rates were calculated based on a specific capacity of 168 mA h g^{-1} for TiO_2, where 1 C corresponds to an applied specific current of 168 mA g^{-1}. In this work, galvanostatic tests were either carried out at 1 or 2 C, explicitly stated in each case.

Results and Discussion

Defining the conditions for operando probing of TiO_2 IO anodes.—The optical probe is based on an angle-resolved transmission measurement arrangement (Fig. 1a) where the TiO_2 IO electrode is measured while charging and discharging in a half-cell arrangement versus lithium metal acting as the counter and reference electrode (Fig. 1b). Here, we analyse TiO_2 IO anodes prepared on glass substrates coated with a thin layer of Ni metal to provide electrical conductivity, acting as a current collector layer while simultaneously maintaining a degree of optical transparency. More detailed information on the choice of materials and electrode design can be found in the Methods section. When dealing with the optical response of PhCs, an important consideration for the location of the photonic stopband is the periodicity of the structure. For IOs, the centre-to-centre pore distance is often used as an indicator of structural periodicity. For our TiO_2 IOs, we measured centre-to-centre pore distances (Fig. 1c) and found they vary in the range 320–330 nm. These TiO_2 IOs were prepared via sol-gel infiltration of PS spheres (see Methods section for further details) with initial diameters in the range 370–380 nm, exhibiting a well-documented uniform shrinkage upon inversion to the IO.[59,60,62] A typical SEM image of a TiO_2 IO following the deposition of a 20 nm Ni metal layer can be seen in Fig. 1e; the deposition of the metal layer through magnetron sputter coating has the effect of thickening the top surface of the IO walls. Additional SEM images for the TiO_2 IO post-cycling can be found in the Supplementary Materials Fig. S2. These TiO_2 IOs electrodes are materials we have investigated for many years and in binder-free and conductive-additive free formulations, they provide very stable multi-thousand cycle life response in standard carbonate electrolytes and offer a reliable and well characterised LIB anode system to carefully extract a correlation between spectroscopic and electrochemical response.

There remain some open questions for IO electrodes, such as how anatase TiO_2 responds to lithiation during a cycle and over long cycling lifetimes, how interconnected porous materials generally behave during initial and longer term cycling in terms of material expansion, the supposed intrinsic benefits of porosity and what changes occur in materials that are relatively stable to long cycle processes. Optical transmission spectra for typical TiO_2 IOs used in this study are shown in Figs. 1d and 1f for a pristine TiO_2 IO in air and a Ni-coated TiO_2 IO in $LiPF_6$ electrolyte, respectively. The photonic stopband for the IO in air at 573 nm red-shifts to 766 nm upon infiltration with electrolyte. This effect is expected due to the increase in the effective refractive index of the IO when the electrolyte replaces the air in the porous structure and the additional Ni metal content.[59,62] The Bragg-Snell model is commonly used to estimate and predict the central position of photonic bandgaps and stopbands.[73–75] At 0° incidence, the minimum transmission wavelength λ_{111} for light reflected from the primary (111) plane is found from the Bragg-Snell relation using the effective refractive index n_{eff}

and the interplanar spacing d_{111} as:

$$\lambda_{min} = 2d_{111}n_{eff} \quad [1]$$

A common method, of which there are a few, used to calculate the n_{eff} is based on a volume averaging of the IO refractive index n_{IO}, with volume fraction φ_{IO} (ideal structure typically, $\varphi_{IO} = 0.26$), and the background filling material refractive index n_{bg}, with volume fraction φ_{bg} (ideal structure typically, $\varphi_{bg} = 0.74$), as:

$$n_{eff} = n_{IO}\varphi_{IO} + n_{bg}\varphi_{bg} \quad [2]$$

Our previous work[60,62,76] with anatase TiO_2 IOs found a good agreement between effective refractive index estimates using Eq. 2 and experimentally measured optical transmission spectra for $n_{IO} = 2.488$, yielding an estimate for the effective refractive index of $n_{eff} = 1.387$. For the primary (111) reflection plane, d_{111} can be calculated for ideal and isotropic PhCs using the centre-to-centre pore distance D via the relation:

$$d_{111} = \sqrt{\frac{2}{3}}D \quad [3]$$

Measurements with TiO_2 IOs show that a reduced interplanar spacing is likely present in TiO_2 IOs prepared using this method[60,62] possibly attributed to anisotropic shrinking of the space between layers when compared to the pore sizes on the horizontal plane. Importantly for this work, any changes to the optical spectra originating from any changes to material dielectric constant, electrolyte or thickness/periodicity are comparative to an initial state or position, allowing for stopband shifts to be simply related to changes in n_{eff} or d_{111}, as in Eq. 1. This work is concerned with shifts to the stopband position and how those shifts can be interpreted for a PhC battery electrode during cycling.

Reversible lithiation that causes cyclic fluctuations in optical transmission.—Since this approach is sensitive to changes in both material refractive index and periodicity/dimension, the fundamental electrochemical response was defined at the outset. Figures 2a and 2b show the voltammetric response observed on a typical cyclic voltammogam (CV) for a TiO_2 IO electrode for the first and second cycle, respectively. The current peaks at ~1.63 V in the cathodic sweep and ~2.20 V in the anodic sweep are typical of reversible lithiation reactions with anatase phase TiO_2,[77] peaks present just below ~1.3 V in the cathodic sweep may suggest the presence of a bronze phase TiO_2(B), potentially indicating a mixture of both phases.[78] However, there is a large peak at ~2.20 V in the cathodic sweep of the first CV cycle which is not present in the second cycle, or any subsequent cycles for that matter. The peak voltage for this reaction coincides with the reported reaction potential for the conversion of Ni metal to NiO;[79] the reverse reaction (NiO conversion to Ni metal) is not present in this potential window (1.0–3.0 V) as this reaction is reported to happen below 1.0 V[79] and so the modification of the Ni current collecting layer would appear to remain unique to the very first cycle.

The operando monitoring of the TiO_2 IO electrode immediately revealed some significant effects on the appearance of the transmission spectra, compared to the initial spectra prior to cycling. One such effect is visible in Figs. 2d and 2e, which show several transmission spectra, recorded at 3.0 V, for two different TiO_2 IO electrodes undergoing cyclic voltammetry (Fig. 2d) and galvanostatic charge/discharge (Fig. 2e). For every electrode we cycled, and every electrochemical process we tested, we find a significant irreversible drop in transmission intensity through the electrode, which occurs after the first cycle and, critically, remains essentially unchanged for all subsequent cycles. The oxidation of the Ni metal current collector layer to NiO is most likely the underlying cause for the significant reduction in transmission intensity unique to the first cycle; the conversion process appears to cease after the first cycle, as per the CV data, with no substantial drops in transmission intensity observed after this point. The photonic stopband also undergoes a considerable red-shift (~16 nm) in the first cycle and importantly, only in the first cycle, between 3.0 V and 2.0 V, again likely linked to the conversion of Ni to NiO and subsequent increase in effective refractive index of the PhC,[76] see Supplementary Materials Fig. S3 for more details on this process.

Intercalation-mode Li-ion battery material involve reversible lithium insertion and removal during each cycle. This often results in volumetric swelling, sometimes causing cracking in cyclic swelling/contraction cycles, among other effects. Determining the relative contributions of composition (thus refractive index) changes and physical (dimension) changes is difficult and they are often measured separately. Our approach couples both parameters and we find that real-time monitoring of these processes exhibits cyclic behavior coincident with the charging and discharging cycles. Figures 2c and 2f show a series of operando transmission spectra recorded at 0.1 V intervals for a typical cathodic sweep (discharge, 3.0 V–1.0 V) and the corresponding anodic sweep (charge, 1.0 V–3.0 V), respectively. Most notably, we see a cyclic fluctuation in the optical transmission intensity of the entire spectrum that is closely linked to the operating voltage. Lithium insertion into the electrode during the discharge acts to decrease the overall transmission intensity. The transmission intensity is then recovered to the initial intensity, at the cycle's beginning, when lithium is removed during the charge process.

Here, this effect is shown for a typical CV cycle (0.2 mV s^{-1}) but we observe this cyclic process in every cycle during voltammetric measurements and also during galvanostatic charge-discharge cycles. The transmission intensity constantly, and reversibly, responds to the operating voltage and thus, the level of lithiation of the electrode i.e. the mole fraction of Li in $Li_\chi TiO_2$. Several of the operando spectra in Figs. 2c and 2f are displayed in color to draw attention to certain spectra at specific voltages, namely, the spectra which coincide with the largest suppression or recovery in transmission intensity. In the discharge in Fig. 2c, the largest drop in transmission intensity is found between 1.7–1.5 V. Likewise, during charging the most pronounced recovery in the transmission intensity is found in the operando spectra recorded between 2.1–2.3 V. Considering that for TiO_2, the lithium insertion reaction in the discharge occurs at ~1.63 V and the lithium removal reaction occurs at ~2.20 V, as per the CV data, there appears to be a strong correlation between the expected mole fraction of lithium content in the electrode and the transmission intensity. Greater lithium mole fractions in the electrode clearly cause a suppression of total optical transmission. It would appear that as the lithium content in TiO_2 increases, greater amounts of reflection, scattering or absorption are associated with the TiO_2 IO electrode and vice-versa. The transmission intensity changes are consistent across multiple cycles. Cyclic opacity in the electrode is thus linked to the state of charge or depth of discharge. For example, during the lithiation of the electrode in the discharge process, voltages between 1.7–1.5 V are the onset of more optically opaque electrodes and this voltage window in a typical galvanostatic discharge process coincides with an increase in the lithium mole fraction in $Li_\chi TiO_2$ from $\chi \sim 0.1$ to $\chi \sim 0.25$, as per Fig. 3a below.

The photonic band-gap and changes to material properties in operando.—Beyond the overall optical transmission intensity changes during cycling, which track the reversible lithiated state of the electrode, spectral features near the photonic band-gap (or photonic stopband in this case) of the ordered macroporous electrode can reveal much finer changes in the optical profile and, as such, the dimensions or material composition changes to the TiO_2 IO. As per Eqs. 1–3 the photonic stopband of PhC materials is inherently sensitive to the IO pore spacing and refractive indices of the materials comprising the porous structure. Figure 3a shows the calculated specific capacity at cycle 7 and cycle 70 for a TiO_2 IO undergoing repeated galvanostatic charge/discharge processes at a

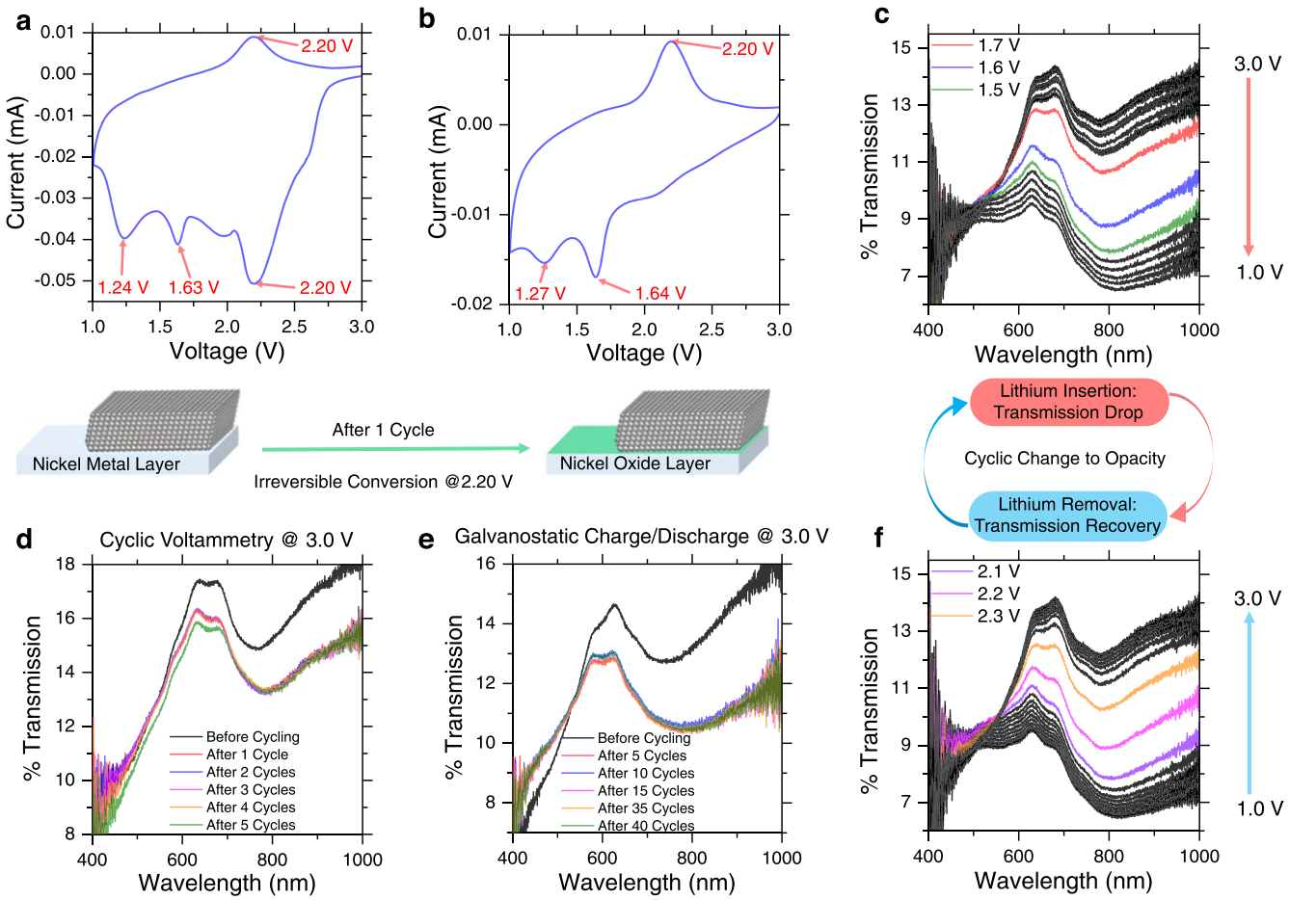


Figure 2. Cyclic optical opacity and lithiation. Labelled peaks on cyclic voltammetry curves for the (a) 1st and (b) 2nd cycles of a typical TiO_2 IO anode, cycled at 0.2 mV s^{-1}, showing the disappearance of a prominent peak centred at 2.20 V after the first discharge with a suggested link to an irreversible conversion of Ni to NiO in the 3.0–1.0 V voltage window. Operando optical spectra recorded for TiO_2 IO anodes at 3.0 V for electrodes undergoing (d) cyclic voltammetry and (e) galvanostatic charge/discharge processes, highlighting an initial significant irreversible drop in transmission intensity occurring in the early stages of battery life. Reversible and cyclic transmission intensity fluctuations shown via operando optical spectra recorded at 0.1 V intervals in a typical (c) discharge (cathodic sweep) and (f) charge (anodic sweep) for a TiO_2 IO anode. Certain spectra are accentuated in color to highlight specific voltage intervals with the largest fluctuations in transmission intensity.

C-rate of 2 C, showing a respectable performance with a discharge specific capacity of ∼160 mA h g^{-1} at that fast rate, comparing favourably with other reports for TiO_2 IO materials[41,42] and our previous examination of these types of electrodes over 5000 cycles; the volumetric expansion is expected to be small in the first several hundred cycles. Figure S13 in the Supplementary Materials show parallel electrochemical tests performed using identical TiO_2 IO electrodes on glass substrates with a Ni metal coating in coin cell apparatus, with very similar electrochemical performances to the flooded cell tests used to record operando optical measurements here. For the data shown in Fig. 3a, calculated mole fractions of lithium incorporation into $Li_\chi TiO_2$ based on the theoretical specific capacity for TiO_2, that is 168 mA h g^{-1} for $Li_{0.5}TiO_2$ or 335 mA h g^{-1} for Li_1TiO_2[23,42] indicate that ∼0.5 moles ($Li_{0.5}TiO_2$) are incorporated at full discharge, a common occurrence with TiO_2 electrodes. Figure 3b shows the corresponding operando optical transmission spectra for cycle 7 and cycle 70, both recorded at 3.0 V. An enlarged view of the photonic stopband is shown in Fig. 3c, showing the subtle changes in the stopband energies during cycling. Most importantly, the shift in the central wavelength position of the photonic stopband is emphasised with ∼10 nm red-shift observed between cycle 7 and 70. Additional operando optical spectra for these measurements, showing the cyclic reversible transmission intensity, can be found in the Supplementary Materials Fig. S4.

Figure 3d depicts the measured stopband minimum, recorded from operando spectra at 3.0 V, versus the number of completed full (charge and discharge) cycles. Interestingly, there appears to be a linear relationship between the stopband position and the number of completed cycles; which would imply that the cycle life of the electrode is indicated by the red-shift in stopband position. Over extended (several hundred to several thousand) cycling periods, the structural walls of TiO_2 IOs have been observed to thicken[42] while retaining the periodicity and interconnected order. Quantifying this change in the IO structure as relating to an expansion of the interplanar spacing of the PhC or an increase in the effective refractive index of the composite material should allow for a correlation to be established between the observed structural color of the material and the cycle number. Expansion occurs in all directions and the change to the stopband energy is linked to the (111) planes of the ordered crystal, i.e. its thickness. The electrochemical behavior of the TiO_2 IO is stable across a number of cycles, as seen in Fig. 3e with consistent specific capacity values (∼150–160 mA h g^{-1}). The Supplementary Material Fig. S5 provides more detail on the Coulombic efficiency for this cell. The red-shift of the photonic stopband appears to be a gradual and consistent process that occurs throughout the battery life, as illustrated in Fig. 3f. Changes to the photonic stopband position are minor, often just a few nanometres of spectral shift, depending on the number of cycles completed. It is important to remember that the cyclic and reversible change in light transmission from reversible lithiation *during* each cycle in Fig. 2 of course happens here also, consistently occurring for every cycle as the operating voltage varies between

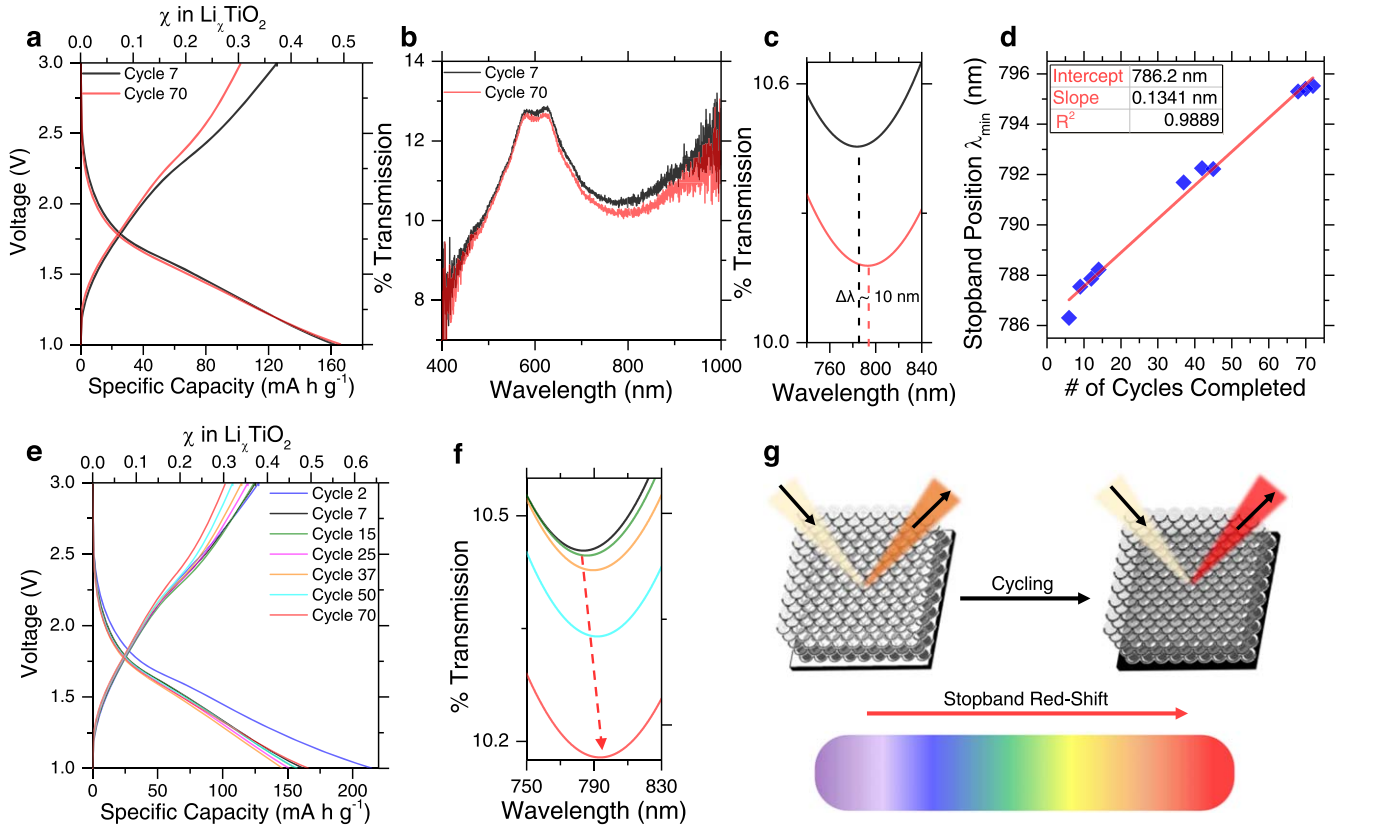


Figure 3. Photonic stopband spectral shift during reversible lithiation. (a) Voltage versus specific capacity for a typical TiO_2 IO anode undergoing galvanostatic charge/discharge cycling at 2 C, showing cycle 7 and cycle 70. (b) The corresponding operando optical transmission spectra, both recorded at 3.0 V. (c) The same optical spectra with a closer focus on the gradual red-shift in stopband position with increased battery cycling, in this case highlighting a 10 nm red-shift recorded between cycle 7 and cycle 70. (d) A plot showing the recorded stopband positions at 3.0 V versus the number of completed cycles for a TiO_2 IO anode at a charge/discharge rate of 2 C. A linear fit is applied to the data, suggesting a predictable red-shift with increasing cycle number. (e) Recorded specific capacity values at 2 C across a number of cycles in the galvanostatic charge/discharge process of a TiO_2 IO anode. (f) Enlarged view of the photonic stopband of a TiO_2 IO anode showing the gradual red-shift in the central stopband position at 3.0 V with higher cycle number. (g) A schematic diagram showing the proposed effect of battery cycling on the photonic stopband of IO structured electrodes, with a red-shift in the optical signature observed for increased cycling.

3.0 V and 1.0 V. Meanwhile, the stopband positions recorded at 3.0 V at the beginning of each cycle appear to red-shift over extended cycling periods, suggesting that the changes to the dimension or refractive index of the TiO_2 active material underlying the red-shift effect become gradually apparent the longer the electrochemical processes persist on the IO material.

This gradual red-shift in stopband position is not limited to galvanostatic charge/discharge processes; it can also be observed in repeated voltammetric cycling. Optically, the operando transmission spectra, recorded at 3.0 V in each case, for a number of selected cycles are shown in Figs. 4a–4c for scan rates of 0.1, 0.2 and 0.3 mV s^{-1}, respectively. For each scan rate, the spectra are compared at 3.0 V after a period of 4 full cycles has passed. Importantly, there is a gradual red-shift in the stopband position with cycle number, observed in each case. At 0.1 mV s^{-1} the stopband shifts ~11 nm from 781 nm to 792 nm between cycle 1 and cycle 5. A smaller stopband shift of ~9 nm from 781 nm to 790 nm between cycle 1 and cycle 5 is observed for the electrode cycled at 0.2 mV s^{-1}. Finally, the smallest stopband shift of ~8 nm from 778.5 nm to 786.5 nm is observed for the electrode cycled at 0.3 mV s^{-1} between cycle 2 and 6. Figures 4d–4f show the recorded CV curves for the 2nd cycle for the three different TiO_2 IO electrodes at scan rates of 0.1, 0.2 and 0.3 mV s^{-1}, respectively. In each case, the most prominent reaction peaks are located at ~1.6 V in the cathodic sweep and ~2.2 V in the anodic sweep, typical of TiO_2 electrodes.[77,78]

By examining the red-shifts, recorded after 4 completed cycles for each scan rate shown in Figs. 4a–4c, a trend in the optical data emerges. The largest red-shift of 11 nm is associated with the slowest scan speed (0.1 mV s^{-1}) and the smallest red-shift is linked to the quickest scan rate (0.3 mV s^{-1}). Extending this analysis to include the stopband red-shift data for additional CV cycles, shows the trend is maintained, as depicted in Fig. 4g. The highest rate of change in the stopband position with cycle number is observed for the slowest scan speed (0.1 mV s^{-1}), featuring the steepest slope of 2.86 nm/cycle, with the converse statement being true for the slowest scan speed with a slope of just 1.60 nm/cycle. Since the potentiodynamic voltammetry does not force a constant reaction rate from a fixed current of a galvanostatic cycle, the fastest scan rate thus corresponds to the shortest lithiation duration. Additionally, the change in scan rate is just 0.1 mV s^{-1}, yet we observe a specific difference in response correlated to the degree of lithiation, showing how sensitive the measurement and lithiation processes are to voltage changes. The extended lithiation period of the overall cycle associated with slower scan speeds may contribute to this effect, with higher degrees of lithiation and repeated cycling causing further red-shifting of the stopband. By comparison to the galvanostatic data in Fig. 2e, we note that the fixed current (reaction rate) under standard charge-discharge conditions results in a stopband shift of ~0.134 nm/cycle, slightly over an order of magnitude less that under voltammetric polarization in spite of a near identical effect of cyclic optical transmission variation during each cycle. Since our method is not susceptible to differences between the cumulative processes that contribute to the total integrated time in galvanostatic vs voltammetric cycling, the difference in stopband shift from changes to material dimension indicates that the galvanostatic data results in a lesser degree of lithiation-induced swelling per cycle than voltammetry under similar conditions.

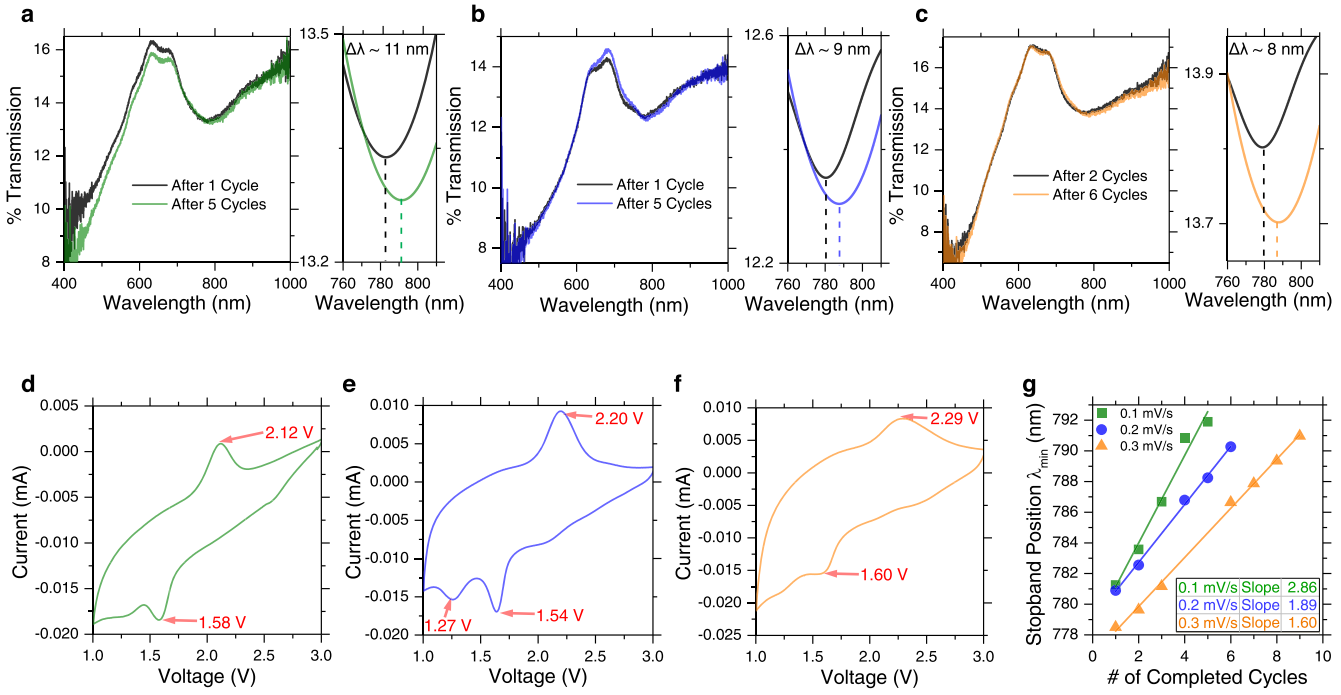


Figure 4. Linking red-shift to electrode cycle life. Gradual red-shifting of the photonic stopband in operando optical spectra of TiO_2 IOs occurring over the course of battery operation for cyclic voltammetry at rates of (a) 0.1 mV s^{-1}, (b) 0.2 mV s^{-1} and (c) 0.3 mV s^{-1}, all spectra shown are recorded at a voltage of 3.0 V. In each case, the shift in stopband position is shown with an accompanying plot where the shift in stopband position is accentuated. The corresponding cyclic voltammetry curves, with labelled reactions peaks, for the same TiO_2 IO anodes in their second cycle recorded at rates of (d) 0.1 mV s^{-1} (e) 0.2 mV s^{-1} and (f) 0.3 mV s^{-1}. (g) A plot of the photonic stopband positions, all recorded at 3.0 V, versus the number of completed CV cycles for TiO_2 IO anodes at three different CV scan rates. The data for the relationship between stopband position and number of completed cycles for fixed scan rate follow a linear fit.

An interesting feature of the plots in Fig. 4g is that there appears to be a strong linear correlation between the shift in stopband position and the number of cycles completed. This effect, for these electrodes with different CV scan speeds, is similar to the linear trend in stopband shift observed in galvanostatic charge/discharge, data displayed in Fig. 3d. From the operando optical data, it would appear that every electrochemical test acts to alter the TiO_2 IO electrode, in a steady and predictable manner, giving rise to the observed photonic stopband red-shift effect. Additional tests performed on TiO_2 IOs prepared from larger polystyrene sphere templates also show the same optical effects; there is a red-shift in the photonic stopband position (now centred at longer wavelengths from a larger initial pore size) with increased cycling. More details on the performance and behavior of the larger pore TiO_2 IO electrodes can be found in the Supplementary Materials Figs. S6–S8. The fact that the stopband red-shifts, regardless of the initial central wavelength position, suggests that this red-shift is closely linked to the properties of the photonic stopband and of the reversibly lithiated electrode as a whole and, critically, not an isolated or abnormal change to the transmission/absorption properties of the material in a specific region of the spectrum. Referring back to Eq. 1, there are two possible explanations for the red-shift in the photonic stopband: an increase in d_{111} (the out-of-plane interplanar spacing of the photonic crystal) or an increase in n_{eff} (the effective refractive index).

Considering the small magnitude of the red-shift to the photonic stopband, changes to either of these parameters would also be minor. In this study, some of the larger shifts in stopband position were on the scale of ~10 nm. In galvanostatic charge/discharge tests a 10 nm stopband red-shift was recorded after 70 cycles compared to just 7 cycles and in CV tests at 0.1 mV s^{-1} a stopband red-shift of 11 nm was recorded between cycle 1 and 5. The corresponding changes to the electrode parameters would equate to $\Delta d_{111} = 3$ nm or $\Delta n_{\text{eff}} = 0.025$, assuming the optical shift can be attributed solely to each parameter and not some combination of both, overall constituting very small changes to the system properties. These miniscule modifications to the electrode system are difficult to detect accurately by experimental means, e.g. in-situ or operando microscopy measurements require sensitivity to track the slight changes to d_{111} which are of the order of ~1% of the overall interplanar spacing of the macroporous electrode, and photoelectron or energy loss spectroscopy analyses of the surface/interface rely on specific cell designs to confidently probe the region of interest. Tomographic or CT-methods could visualise structural changes, but the sensitivity of the spectral shifts used in this work provide high fidelity tracking of very small, but systematic, changes to the overall electrode during each cycle, and over the full cycle life, both together. Consequently, for the TiO_2 IO electrode system examined here, it is currently difficult to uncouple the minor shift in photonic stopband position and attribute its origin to either a change in d_{111} or n_{eff}, or, some combination of both parameters.

The PhC electrodes examined in this work consisted of 8–10 layers of IO material (see Supplementary Materials Fig. S7, for example). Assuming a change in the structural periodicity of $\Delta d_{111} =$ 3 nm alone is responsible for the photonic stopband shift, this would translate to a maximum increase in the overall height of the electrode of approximately 24–30 nm. Some measured expansion of the electrode height would indicate a change to d_{111}, otherwise a change to n_{eff} could be assumed. Considering changes to n_{eff} as the source of the photonic stopband red-shift, one possibility to consider for the proposed increase in n_{eff} is the formation of the SEI layer on the surface of TiO_2 anode. The relatively small increase in the refractive index ($\Delta n_{\text{eff}} \sim 0.025$) needed to achieve a red-shift of approximately 10 nm may originate from an increase in refractive index associated with an expanding SEI layer. However, the red-shift of the stopband observed from operando measurements appears to progress linearly with cycle number, implying that the SEI layer would evolve linearly also. When considering SEI layer formation, larger contributions to the layer composition would likely be expected in earlier cycles as the layer stabilises over time, projecting a non-linear

evolution of the SEI layer, contrasting the linear spectral red-shifts reported here.

Overall, the observations reported in this work show a very sensitive change to the optical transmission of an electrode that is linked to the state of charge or depth of discharge (and lithium mole fraction) within each cycle. In addition, we can also track a small but systematic change to the periodicity / thickness or material composition / refractive index of an electrode in real-time from the shift of the photonic stopband of an IO-structured TiO_2 electrode. Within each red-shifted cycle, the remarkably consistent reversible and cyclic change to transmission intensity during the cycle is always maintained and this is found under galvanostatic and voltammetric conditions. The operando optical effects observed here during reversible lithiation are fascinating and have the potential to offer an optical real-time readout of electrode state based on an observed structural color. The method allows the reversibility to be tracked during each cycle and the state of the electrode to be monitored over extended cycling non-destructively, which may prove useful for materials sensitive to swelling, changes in electronic conductivity or mechanical integrity with lithiation, or for assessing the influence of SEI, CEI or other interfacial films or interphases developing during the cycle of an electrode.

Conclusions

Operando optical transmission spectra in conjunction with electrodes adopting an IO design, provides real-time optical sensing of the degree of lithiation and electrode cycling behavior. Through close monitoring of the transmission spectra during operation, the operando optical spectra reveal an intricate relationship between the magnitude of the transmission intensity and the nominal lithium content expected in the electrode at various operating voltages. Drops in the overall transmission intensity correlate to higher uptake of lithium content in the electrode; a remarkable reversibility is seen in the inverse process as the intensity recovers at the onset of voltages corresponding to lithium extraction from the electrode. Cyclic variability in the optical transmission intensity is shown to relate directly to the state of charge of the electrode, linking the electrode optics to the electrochemical performance.

Another optical effect which shows great promise is the structural color inherent to the IO PhC, exhibiting a direct response to repeated cycling. A gradual red-shift of the photonic stopband is incurred over the course of multiple cycles, establishing a visual color indicator of the electrode behavior and history. From the data sets reported here, it would appear that this shift in stopband position is linear with cycle number and, more importantly, predictable. An observable structural color for an electrode linked to the cycle number has the potential to chronicle the electrochemical performance, provided the optical behavior of the IO material is reasonably well-understood and characterized. Taking the broad applicability of this technique into consideration, with it being feasible for a wide range of electrode materials which can adopt an IO structure or be constructed as some form of PhC with an observable structural color, the operando optical analysis explored here is versatile enough to inform on electrode phase and structural evolution while relating this information back to expected levels of lithiation during the cycle. This method shows great promise in assessing and diagnosing material performance, furthering our understanding of potential electrode material candidates by closely monitoring their fundamental material properties alongside their electrochemical evolution.

Acknowledgments

Support from the Irish Research Council Advanced Laureate Award under grant no. IRCLA/2019/118, Government of Ireland Postgraduate Scholarship under award no. GOIPG/2016/946, and a Government of Ireland Postdoctoral Fellowship under award no. GOIPD/2021/438 is gratefully acknowledged. We also acknowledge support from the European Union's Horizon 2020 research and innovation program under grant agreement No 825114.

ORCID

Alex Lonergan https://orcid.org/0000-0003-4949-1181
Colm O'Dwyer https://orcid.org/0000-0001-7429-015X

References

1. T. Kim, W. Song, D.-Y. Son, L. K. Ono, and Y. Qi, *J. Mater. Chem. A*, **7**, 2942 (2019).
2. F. Wu, J. Maier, and Y. Yu, *Chem. Soc. Rev.*, **49**, 1569 (2020).
3. M. S. Ziegler and J. E. Trancik, *Energy Environ. Sci.*, **14**, 1635 (2021).
4. D. Chen, Z. Lou, K. Jiang, and G. Shen, *Adv. Funct. Mater.*, **28**, 1805596 (2018).
5. L. Kong, C. Tang, H.-J. Peng, J.-Q. Huang, and Q. Zhang, *SmartMat*, **1**, 1 (2020).
6. H. Kim, W. Choi, J. Yoon, J. H. Um, W. Lee, J. Kim, J. Cabana, and W.-S. Yoon, *Chem. Rev.*, **120**, 6934 (2020).
7. F. Wang, B. Wang, J. Li, B. Wang, Y. Zhou, D. Wang, H. Liu, and S. Dou, *ACS Nano*, **15**, 2197 (2021).
8. J.-L. Shi et al., *Adv. Mater.*, **30**, 1705575 (2018).
9. A. Manthiram, *Nat. Commun.*, **11**, 1550 (2020).
10. N. Mahmood, T. Tang, and Y. Hou, *Adv. Energy Mater.*, **6**, 1600374 (2016).
11. L. Zhang, X. Qin, S. Zhao, A. Wang, J. Luo, Z. L. Wang, F. Kang, Z. Lin, and B. Li, *Adv. Mater.*, **32**, 1908445 (2020).
12. M. Osiak, H. Geaney, E. Armstrong, and C. O'Dwyer, *J. Mater. Chem. A*, **2**, 9433 (2014).
13. E. Pomerantseva, F. Bonaccorso, X. Feng, Y. Cui, and Y. Gogotsi, *Science*, **366**, eaan8285 (2019).
14. J. Xu, R. D. Deshpande, J. Pan, Y.-T. Cheng, and V. S. Battaglia, *J. Electrochem. Soc.*, **162**, A2026 (2015).
15. H. Liu, M. Wolfman, K. Karki, Y.-S. Yu, E. A. Stach, J. Cabana, K. W. Chapman, and P. J. Chupas, *Nano Lett.*, **17**, 3452 (2017).
16. N. Iqbal, I. U. Haq, and S. Lee, *Int. J. Mech. Sci.*, **216**, 107034 (2022).
17. D. Liu et al., *Adv. Mater.*, **31**, 1806620 (2019).
18. H. Li, S. Guo, and H. Zhou, *Journal of Energy Chemistry*, **59**, 191 (2021).
19. A. Grant and C. O'Dwyer, *Appl. Phys. Rev.*, **10**, 011312 (2023).
20. P. P.-R. M. L. Harks, F. M. Mulder, and P. H. L. Notten, *J. Power Sources*, **288**, 92 (2015).
21. R. van de Krol, A. Goossens, and E. A. Meulenkamp, *J. Electrochem. Soc.*, **146**, 3150 (1999).
22. S. Misra, N. Liu, J. Nelson, S. S. Hong, Y. Cui, and M. F. Toney, *ACS Nano*, **6**, 5465 (2012).
23. K. Li, B. Li, J. Wu, F. Kang, J.-K. Kim, and T.-Y. Zhang, *ACS Appl. Mater. Interfaces*, **9**, 3322917 (2017).
24. B. R. Long, M. K. Y. Chan, J. P. Greeley, and A. A. Gewirth, *The Journal of Physical Chemistry C*, **115**, 1122916 (2011).
25. M. Kitta and H. Sano, *Langmuir*, **33**, 1861 (2017).
26. Q. P. McAllister, K. E. Strawhecker, C. R. Becker, and C. A. Lundgren, *J. Power Sources*, **257**, 380 (2014).
27. N. M. Trease, L. Zhou, H. J. Chang, B. Y. Zhu, and C. P. Grey, *Solid State Nucl. Magn. Reson.*, **42**, 62 (2012).
28. P. Hovington, M. Dontigny, A. Guerfi, J. Trottier, M. Lagacé, A. Mauger, C. M. Julien, and K. Zaghib, *J. Power Sources*, **248**, 457 (2014).
29. Z. Fan, L. Zhang, D. Baumann, L. Mei, Y. Yao, X. Duan, Y. Shi, J. Huang, Y. Huang, and X. Duan, *Adv. Mater.*, **31**, 1900608 (2019).
30. F. Shi, P. N. Ross, G. A. Somorjai, and K. Komvopoulos, *The Journal of Physical Chemistry C*, **121**, 1122476 (2017).
31. A. G. Hsieh, S. Bhadra, B. J. Hertzberg, P. J. Gjeltema, A. Goy, J. W. Fleischer, and D. A. Steingart, *Energy Environ. Sci.*, **8**, 1569 (2015).
32. A. J. Merryweather, C. Schnedermann, Q. Jacquet, C. P. Grey, and A. Rao, *Nature*, **594**, 522 (2021).
33. A. J. Merryweather, Q. Jacquet, S. P. Emge, C. Schnedermann, A. Rao, and C. P. Grey, *Nat. Mater.*, **21**, 1306 (2022).
34. R. Pandya et al., *Nat. Nanotechnol.*, **18**, 1185 (2023).
35. R. Pandya, A. Mathieson, B. D. Boruah, H. B. de Aguiar, and M. de Volder, *Nano Lett.*, **23**, 7288 (2023).
36. L. Albero Blanquer, F. Marchini, J. R. Seitz, N. Daher, F. Bétermier, J. Huang, C. Gervillié, and J.-M. Tarascon, *Nat. Commun.*, **13**, 1153 (2022).
37. C. Hogrefe, T. Waldmann, M. B. Molinero, L. Wildner, P. Axmann, and M. Wohlfahrt-Mehrens, *J. Electrochem. Soc.*, **169**, 050519 (2022).
38. D. Zhang, R. Wang, X. Wang, and Y. Gogotsi, *Nature Energy*, **8**, 567 (2023).
39. L. Kavan, M. Zukalová, M. Kalbáč, and M. Graetzel, *J. Electrochem. Soc.*, **151**, A1301 (2004).
40. J. S. Sakamoto and B. Dunn, *J. Mater. Chem.*, **12**, 2859 (2002).
41. D. McNulty, A. Lonergan, S. O'Hanlon, and C. O'Dwyer, *Solid State Ionics*, **314**, 195 (2018).
42. D. McNulty, E. Carroll, and C. O'Dwyer, *Adv. Energy Mater.*, **7**, 1602291 (2017).
43. X. Huang, J. Chen, Z. Lu, H. Yu, Q. Yan, and H. H. Hng, *Sci. Rep.*, **3**, 2317 (2013).
44. M. Zhou, Y. Xu, C. Wang, Q. Li, J. Xiang, L. Liang, M. Wu, H. Zhao, and Y. Lei, *Nano Energy*, **31**, 514 (2017).
45. A. Esmanski and G. A. Ozin, *Adv. Funct. Mater.*, **19**, 1999 (2009).
46. J.-H. Jeong, K.-H. Kim, D.-W. Jung, K. Kim, S.-M. Lee, and E.-S. Oh, *J. Power Sources*, **300**, 182 (2015).
47. T. Song et al., *Energy Environ. Sci.*, **5**, 9028 (2012).
48. S. Geier, R. Jung, K. Peters, H. A. Gasteiger, D. Fattakhova-Rohlfing, and T. F. Fässler, *Sustainable Energy & Fuels*, **2**, 85 (2018).

49. D. McNulty, H. Geaney, Q. Ramasse, and C. O'Dwyer, *Adv. Funct. Mater.*, **30**, 2005073 (2020).
50. M. Agrawal, S. Choudhury, K. Gruber, F. Simon, D. Fischer, V. Albrecht, M. Göbel, S. Koller, M. Stamm, and L. Ionov, *J. Power Sources*, **261**, 363 (2014).
51. H. Liu, H.-M. Cho, Y. S. Meng, and Q. Li, *ACS Appl. Mater. Interfaces*, **6**, 9842 (2014).
52. D. Gueon, D.-Y. Kang, J. S. Kim, T. Y. Kim, J. K. Lee, and J. H. Moon, *J. Mater. Chem. A*, **3**, 222684 (2015).
53. D. Li, W. Zhang, R. Sun, H.-T.-H. Yong, G. Chen, X. Fan, L. Gou, Y. Mao, K. Zhao, and M. Tian, *Nanoscale*, **8**, 112202 (2016).
54. Z. Liang, G. Zheng, W. Li, Z. W. Seh, H. Yao, K. Yan, D. Kong, and Y. Cui, *ACS Nano*, **8**, 5249 (2014).
55. Z. Li, M. Xiao, Y.-F. Liu, H.-H. Gao, and P. V. Braun, *Ceram. Int.*, **47**, 222381 (2021).
56. E. Armstrong and C. O'Dwyer, *J. Mater. Chem. C*, **3**, 6109 (2015).
57. A. Lonergan and C. O'Dwyer, *Adv. Mater. Technol.*, **8**, 2201410 (2022).
58. K. Zhu, C. Fang, M. Pu, J. Song, D. Wang, and X. Zhou, *Journal of Materials Science & Technology*, **141**, 78 (2023).
59. R. C. Schroden, M. Al-Daous, C. F. Blanford, and A. Stein, *Chem. Mater.*, **14**, 3305 (2002).
60. A. Lonergan, D. McNulty, and C. O'Dwyer, *J. Appl. Phys.*, **124**, 095106 (2018).
61. G. I. N. Waterhouse, W.-T. Chen, A. Chan, and D. Sun-Waterhouse, *ACS Omega*, **3**, 9658 (2018).
62. A. Lonergan, C. Hu, and C. O'Dwyer, *Phys. Rev. Mater.*, **4**, 065201 (2020).
63. H. Li, L. Chang, J. Wang, L. Yang, and Y. Song, *J. Mater. Chem.*, **18**, 5098 (2008).
64. V. L. Alexeev, S. Das, D. N. Finegold, and S. A. Asher, *Clin. Chem.*, **50**, 2353 (2004).
65. H. Hu, Q.-W. Chen, J. Tang, X.-Y. Hu, and X.-H. Zhou, *J. Mater. Chem.*, **22**, 112048 (2012).
66. C. E. Lee, T. H. Park, S. Mun, Y. Jung, S. Lee, J. Jang, D. Y. Ryu, and C. Park, *Adv. Mater. Technol.*, **7**, 2200385 (2022).
67. H. Huang, H. Li, X. Shen, K. Gu, J. Guo, and C. Wang, *Chem. Eng. J.*, **429**, 132437 (2022).
68. J. I. L. Chen, G. von Freymann, S. Y. Choi, V. Kitaev, and G. A. Ozin, *Adv. Mater.*, **18**, 1915 (2006).
69. X. Zheng, S. Meng, J. Chen, J. Wang, J. Xian, Y. Shao, X. Fu, and D. Li, *The Journal of Physical Chemistry C*, **117**, 222263 (2013).
70. L. T. Varghese, Y. Xuan, B. Niu, L. Fan, P. Bermel, and M. Qi, *Adv. Opt. Mater.*, **1**, 692 (2013).
71. Y. Zuo, W. Zhang, M. Wei, P. Zhang, S. Zhao, P. Pei, L. Qiu, H. Wang, Z. Meng, and K. Wang, *Energy Storage Mater.*, **53**, 136 (2022).
72. C. O'Dwyer, *Adv. Mater.*, **28**, 5681 (2016).
73. K. Liu, T. A. Schmedake, and R. Tsu, *Phys. Lett. A*, **372**, 4517 (2008).
74. M. Bardosova, M. E. Pemble, I. M. Povey, and R. H. Tredgold, *Adv. Mater.*, **22**, 3104 (2010).
75. A. Grant, A. Lonergan, and C. O'Dwyer, *Opt. Mater.*, **142**, 114053 (2023).
76. A. Lonergan, B. Murphy, and C. O'Dwyer, *ECS J. Solid State Sci. Technol.*, **10**, 085001 (2021).
77. X. Gao, H. Zhu, G. Pan, S. Ye, Y. Lan, F. Wu, and D. Song, *J. Phys. Chem. B*, **108**, 2868 (2004).
78. B. Laskova, M. Zukalova, A. Zukal, M. Bousa, and L. Kavan, *J. Power Sources*, **246**, 103 (2014).
79. J. Ou, S. Wu, L. Yang, and H. Wang, *Acta Metallurgica Sinica (English Letters)*, **35**, 212 (2022).